Title
Repairable and Reconfigurable Structured Liquid Circuits

Journal
Advanced Functional Materials, 34(38)

ISSN
1616-301X

Authors
Fink, Zachary
Kim, Paul Y
Han, Jiale
et al.

Publication Date
2024-09-01

DOI
10.1002/adfm.202402708

Repairable and Reconfigurable Structured Liquid Circuits

Zachary Fink[1], Paul Y. Kim[2], Jiale Han[3], Xuefei Wu[2], Derek Popple[2], Shipei Zhu[2], Han Xue[2], Alex Zettl[2,4], Paul D. Ashby[5], Brett A. Helms[5], Thomas P. Russell[1,2,6*]

AUTHOR ADDRESS

[1] Department of Polymer Science and Engineering, University of Massachusetts Amherst, Amherst, Massachusetts 01003, USA

[2] Materials Sciences Division, Lawrence Berkeley National Laboratory, Berkeley, California 94720, USA

[3] Department of Materials Science and Engineering, University of California, Berkeley, Berkeley, CA 94720, USA

[4] Department of Physics, University of California, Berkeley, Berkeley, CA 94720, USA

[5] Molecular Foundry, Lawrence Berkeley National Laboratory, Berkeley, California 94720, USA

[6] Advanced Institute for Materials Research (WPI-AIMR), Tohoku University, 2-1-1 Katahira, Aoba, Sendai 980-8577, Japan

Keywords: Reconfigurable, 3D printing, liquid electronics, sulfonated PANI, structured liquid

ABSTRACT

The advance of printed electronics has been significantly bolstered by the development of liquid-state electronics that overcome the inherent limitations in flexibility and reconfigurability of solid-state electronics. By integrating the biocompatibility and conductivity of sulfonated polyaniline (S-PANI) and phytic acid (PA) with the reconfigurability of structured liquids, we developed highly conductive all-liquid threads. The dense packing and overlap of PA/S-PANI complexes at an oil/water interface promotes in-plane electron transport, and standard four-point probe measurements of PA/S-PANI interfacial assemblies demonstrate enhanced electrical properties. Notably, the rapid jetting of the ink phase into the matrix phase allows for all-liquid threads to be printed, enabling the fabrication of large-scale, conductive pathways between two electrodes and liquid circuits. Upon mechanical cleavage of the liquid wires, circuits can be broken, but will easily self-

repair using an electric field, making this motif useful in the design of switches as well as restoring conductive pathways in series or in parallel. The demonstrated flexibility and reconfigurability these PA/S-PANI wires possess hold significant promise for their practical use in the design of flexible and adaptive bioelectronics that can be repaired on demand, signifying a transformative step in the evolution of liquid electronic materials.

1. Introduction

The rapid progression of printed electronics has led to tremendous advances in integration, processing speed, and miniaturization.[1–3] However, these strides, primarily based on solid-state components, grapple with inherent limitations in terms of reconfigurability and recyclability.[3,4] Existing attempts by solid electronics to navigate these issues often fall short due to the limited flexibility, the lack of solutions for end-of-life recycling, and the dependence on solid substrates or encapsulation, which fundamentally restricts reconfigurability.[4] These challenges have stimulated studies beyond solid-state components, namely to liquid electronics, which have demonstrated promising results with the development of conductive hydrogels,[5–8] liquid metals,[9–13] and ionic liquid and other liquid electrolyte materials.[14–16] Conductive polymers such as polypyrrole (PPy), polyaniline (PANI) and poly-(3,4-ethylenedioxythiophene) (PEDOT)[6] along with liquid metal alloys[12] composed of gallium, indium, and tin (Galinstan)[17] have opened opportunities for three-dimensional (3D) printing of conductive liquids. These materials are known to exhibit flexibility, and printability[8, 18] that make them ideal for innovative liquid electronic devices.[4, 19]

3D conductive hydrogels are typically generated using an ink phase that contains electrically conductive materials (e.g., conductive polymers or metal nanoparticles) alongside a component crosslinked immediately after the ink is extruded out of the nozzle to form robust, conductive hydrogel structures for printing.[20–22] These structures can be designed to

self-heal if orthogonal chemistries for dynamic covalent bonding are incorporated into the multicomponent structure, but can sometimes require specific environmental conditions (pH, light, temperature, salt, etc.) to obtain the self-healing.[5, 23] Liquid metals are an alternative class of materials that are known for their excellent conductivity and malleability. These materials have a unique property that allows them to remain liquid at room temperature, making them ideal for use in various electronic applications.[4, 9–11, 24] 3D printing with liquid metals can create intricate electronic devices not manufacturable with traditional techniques like metal stamping, casting, and sintering. However, the use of these materials introduces a new set of complications, including the requirement for polymer encapsulation/chemistry for crosslinking, the use of rare elements, and the continued reliance on traditional solid-state electronics architectures.

Our previous research capitalized on the interfacial assembly of functionalized nanoparticle surfactants (NPSs) to generate dense, mechanically stable interfaces such that 3D structured liquid constructs[25–27] could be printed. The assembly and jamming of NPSs, formed from the electrostatic interaction of NPs and ligands that bear complementary functional groups (i.e., COOH and NH_2), significantly increases the binding energy of the NPs to the interface, preventing desorption, and affording mechanically robust interfaces that can suppress Plateau–Rayleigh instabilities.[28] The range of liquid structures that can be generated by this printing technique is broad, and the objects produced have a range of optical, chemical, and physical properties. One advantage of using the structured liquid approach, in the context of 3D printing, is that crosslinking reactions in the bulk solution are completely circumvented, greatly expanding the materials that can be used in the ink phase. Another significant advantage is that the printed structures have a liquid core, making reconfigurability trivial. Notably, we have been able to use negatively charged MXene flakes and complementary amine ligands to form a densely packed MXene interface[4, 29, 30] between the

ink and matrix phases generating all-liquid, 3D printed conductive devices that could activate an LED.[4] While the performance and control over device configuration of the MXene devices were excellent, they still incorporated metal conducting elements in the MXene, detracting from their biocompatibility and environmental friendliness. Reconfiguration was demonstrated by the physical reconnection/re-extrusion of the liquid wires.

To further expand the NPSs platform in generating conductive interfaces, and in an effort to use all organic conducting materials, we show that integrating phytic acid (PA) and sulfonated polyaniline (S-PANI), materials with excellent electrochemical properties,[31–33] into the ink phase can generate conductive all-liquid wires. To generate the structured liquid, the negatively charged S-PANI/PA in the aqueous ink phase electrostatically interacts with positively charged aminated polyhedral oligomeric silsesquioxane (POSS-NH_2) in the oil phase at the interface to form dense, mechanically robust interfacial assemblies. PANI, renowned for its high conductivity, environmental compatibility, and superior electromagnetic interference (EMI) shielding capabilities,[34] can be doped with PA, an acid with multiple anionic phosphate groups, to enhance the conductivity and stability of PANI constructs at the interface. The combination of PANI and PA has been used in conductive hydrogels,[32, 35] for energy storage, and in the textile industry[36, 37] for high performance flexible electronic devices. To develop highly conductive all-liquid wires, it becomes imperative to integrate and distinguish between ionic and electrical conductivity, where ionic conductivity relies on the movement of large charged ion species, while electrical conductivity relies on the movement of electrons. It is worth noting that ionic conductivity likely makes a smaller contribution to the overall conductivity, primarily due to the inherently slower movement of ions compared to the transport of electrons (as is true in water and many other similar liquids). Consequently, PA functions as a physical crosslinker at the interface and creates a more electrically conductive interface due to the interfacial jamming of the PA/S-PANI, a significant benefit for

generating all-liquid wires. Here the ionic conductivity is governed by the movement of charged species (PA ions and S-PANI), while the electrical conductivity may be introduced from the overlapping of S-PANI complexes at the dense oil-water interface.

By optimizing the properties imparted to the liquid materials and interfacial structures by varying the PA and S-PANI concentrations, we developed reconfigurable and highly conductive all-liquid wires with 3D printing, which can be used as an alternative to conventional solid-state electronics. Our research paves the way for a plethora of applications across various fields, including wearable technology, bioelectronics, and flexible electronics, among others.[38, 39]

2. Results and Discussion

2.1 S-PANI Synthesis and Bulk Solution Characterizations

The chemical oxidative polymerization of aniline monomer, under acidic and cold (5°C) conditions, was performed to synthesize polyaniline in its emeraldine salt form, using ammonium persulfate. The emeraldine salt was reduced to its leucoemeraldine base form using phenyl hydrazine. Sulfonation of the polymer product was achieved using a method developed previously by Wei et al.,[40, 41] and the product was then dialyzed to remove impurities (see Fig. 1a and Methods for further details). Fourier-transform infrared spectroscopy (FT-IR) of the dried polymer was used to confirm successful sulfonation, as indicated from the S–C stretching and vibrational absorption peaks observed at 1070, 704, and 610 cm^{-1} [42] (Figure S1), which are characteristic of SO_3 groups substituted on phenyl rings. We also note that the dried polymer could be dissolved in deionized water, a characteristic attained due to the charged nature of the sulfonated polymer, as further evidence of successful sulfonation.

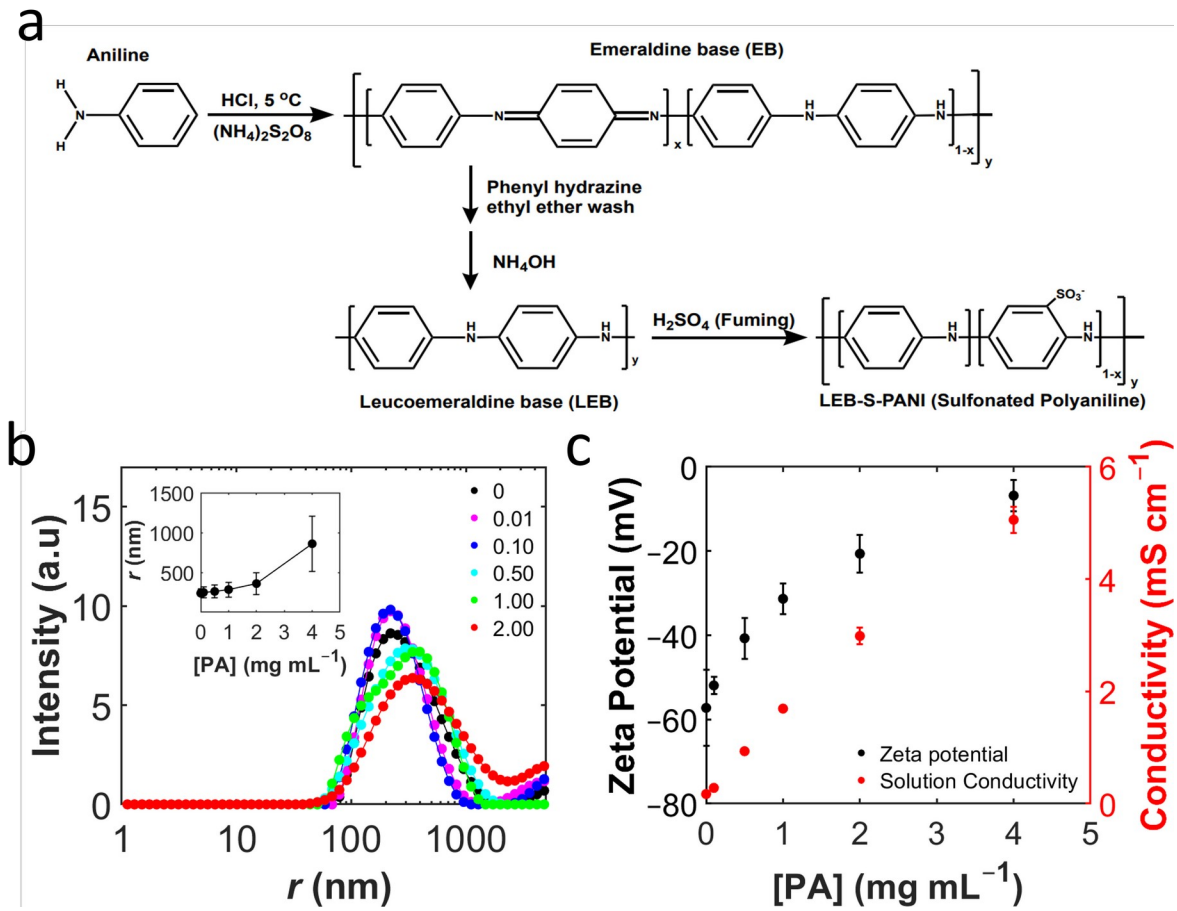

Figure 1: Synthesis and bulk solution characterization of PA doped S-PANI complexes. (a) Synthesis of S-PANI from aniline. (b) DLS measurements of PA/S-PANI NP size using 1 mg mL^{-1} S-PANI as a function of PA concentration (0–4 mg mL^{-1}). (c) Zeta potential and solution conductivity of PA/S-PANI as function of PA concentration.

S-PANI can form self-doped, stable 6-member rings in solution that can make the relationship between concentration and molecular size more complex. To elucidate the size of these self-doped S-PANI particles in solution, dynamic light scattering (DLS) was used to determine the hydrodynamic radius *r* as a function of PA concentration (Fig. 1b). In this case, PA acts to both increase the pH and to physically crosslink S-PANI, as it is well known that the phosphate groups of the PA interact with the nitrogen in PANI polymers. While the addition of PA can lead to large, unstable aggregates if too much PA is added, it also increases the conductivity of the PA/PANI solutions and hydrogel structures.[32, 43, 44] Fig. 1b shows the NP size of the PA/S-PANI complexes while varying PA concentrations from 0–4 mg mL^{-1} and fixed S-PANI concentration of 0.5 mg mL^{-1}. As the PA concentration increased,

the intensity averaged NP size increased, as indicated by the peak shifting towards higher values of *r*, steadily from 234 nm to 360 nm between 0–2 mg mL^{-1}. However, at a concentration of 4 mg mL^{-1}, *r* increased significantly to 860 nm with a broad size distribution, suggesting the formation of large, unstable aggregates in solution. As indicated in Figure 1b, aggregates begin to form even at low PA concentration and the size of the aggregates are likely kinetically controlled. Since there is no characteristic dimension limiting the size of these PA/S-PANI complexes, and the very broad sizes seen in Figure 1b, it is likely that the aggregates form randomly. These large aggregates eventually fall out of solution to the bottom of the solution vial after three to four hours, as shown in Fig S2, with sample that have larger PA concentrations showing much more sedimentation. Solutions with 2 mg mL^{-1} PA and lower remained stable for more than two weeks without requiring additional mixing.

This phenomenon can be attributed to the net charge on the polymer chains as the interactions between PA/S-PANI complexes increasingly lead to reduced zeta potential values as seen in Fig. 1c (left axis). Here, the S-PANI with no PA has a zeta potential of –57.3 mV but decreases to –20 mV at 2 mg mL^{-1}, which is still likely to be stable in solution, but decreases further to –6.8 mV at 4 mg mL^{-1}, indicating weak charge repulsion between the PA/S-PANI complexes. Consequently, the complexes begin to aggregate more and fall out of suspension. The complex interplay between PA content and the ratio of PANI substituents sulfonated on each chain may affect the structural order of the PA/S-PANI and may play a role in the solution aggregation at high PA concentrations. The higher PA content appears to structurally order, more than likely a consequence of the significant steric effect of PA molecules and the strong interactions between PA and PANI chains.[45] The ionic conductivity of the bulk solution was also tested, and, as expected, the trend in Fig. 1c (right axis) shows that the conductivity increased from 0.17 to 5.06 mS cm^{-1} as the PA concentration increased from 0 to 4 mg mL^{-1}. The combination of stability, broad distribution in PA/S-PANI NP size,

and conductivity demonstrate successful control over the solution properties necessary for the rapid stabilization of an oil–water interface when the PA/S-PANI solutions are put into contact with oil containing POSS-NH_2 stabilizing surfactants.

2.2 Interfacial Assembly of PA/S-PANI at an Oil–Water Interface

The characterization of NPs size in the bulk aqueous solution is important, as the stability of the interface relies on the rate of adsorption to the oil–water interface as well as the degree of NP aggregation. Figure 2a schematizes the interfacial assembly at the boundary between PA/S-PANI aqueous solution and silicone oil containing POSS-NH_2 ligands after forming a densely packed interface in a pendant drop geometry. The binding energy of NPs to the interface can be significantly enhanced when negatively charged NPs (S-PANI) in ink phase, interact with positively charged ligands in the immiscible matrix phase (5 cSt silicone oil) at the interface, forming what is commonly referred to as nanoparticle surfactants (NPSs). POSS-NH_2 ligands have native surfactant characteristics and readily assemble at the negatively charged oil–water interface,[46–49] effectively protonating the pendant amines (pKa ~9) near the ink phase (pH 1–4 depending on PA concentration). Subsequently, the S-PANI NPs migrate to the interface due to electrostatic interactions, forming strong ionic bonds with the ligands to create the NPSs. The densely packed nature of the interface, with S-PANI aggregate structures at the interface similar those proposed by Pan et. Al,[32] is beneficial for the electronic properties of the interfacial films since charge transport in the plane of the interface is made much

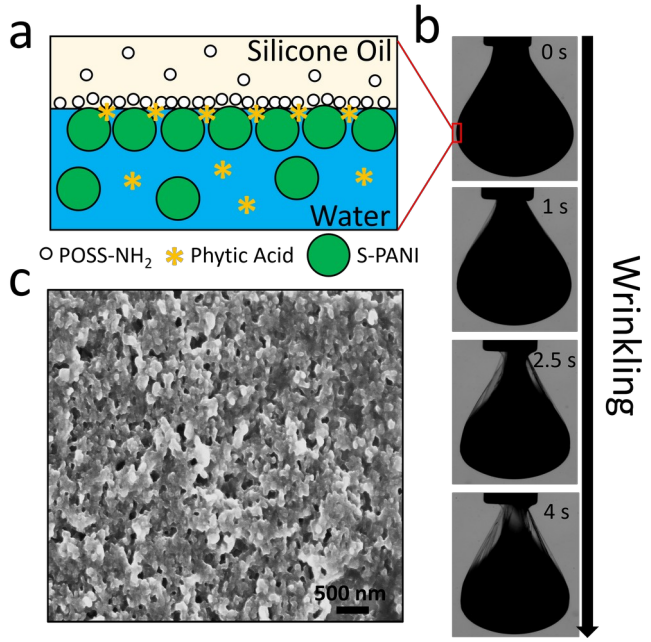

Figure 2: Illustration of interfacial assembly behavior and morphology. (a) Schematic of PA/S-PANI NPs and POSS-NH_2 assemble at interface, noting that PA will also be located within

easier. Therefore, the stability of NPSs at the jammed interface plays a key role in determining the conductivity performance of liquid electronics. In addition to the NPS nature of the S-PANI and POSS-NH_2, PA also assembles at the interface and further increases the conductivity of the interface as a result of the physical crosslinking of PA/S-PANI complexes at the interface and can also increase the ionic conductivity in the bulk aqueous solution.

To understand the interfacial properties at play, interfacial tension (IFT) measurements were conducted using controlled amounts of S-PANI, PA, and POSS-NH_2. Control experiments where no stable assembly is expected was conducted by testing the bare water–silicone oil, S-PANI ink–silicone oil (no POSS-NH_2), PA solution–silicone oil (no POSS-NH_2), and a water–silicone oil (0.5 mg mL^{-1} POSS-NH_2). As expected, the IFT remains constant as a function of time for the control systems (Fig. S3a) with the exception of the sample with POSS-NH_2, which show as slow decrease in IFT from 40 mN m^{-1} to 33 mN m^{-1} over 300 s. However, when placing the PA and S-PANI aqueous phase in contact with 0.5 mg mL^{-1} POSS-NH_2, the dynamic interfacial tension, shown in Fig. S3b, rapidly decreases over the first 10 seconds, from ~ 30 mN m^{-1} to ~ 10–15 mN m^{-1}. The IFT for PA concentrations between 0.5 and 2 mg/ml reach almost the same IFT, suggesting PA is present and is saturated at the interface. This decrease is followed by a more gradual leveling off over time, and reaches a quasi-equilibrium state after 300 s to a value that depends on the specific PA and S-PANI concentrations. This trend holds true over a broad range of PA concentrations (0.01–4 mg mL^{-1}).

The rate of NP attachment to the interface is contingent on the size of the PA/S-PANI complexes and the available interfacial area. Because the size distribution of these PA/S-PANI complexes is large, as indicated by the DLS experiments, it is likely that the smallest PA/S-PANI complexes reach the interface first as a result of diffusion-controlled adsorption. Noticeably, the fastest reduction in IFT is attained for PA/S-PANI ink phases, and reaches very

low IFT values (~8 mN m^{-1}) within seconds, indicating the possibility for 3D printing.[50] A quick measure of the apparent surface coverage, measured as the ratio between the droplet interfacial area when films/wrinkles appear (S_w) upon interfacial area reduction and the initial interfacial area of the droplet (S_0), can be attained from the wrinkling experiment in Fig. 2b. Here, a 2 mg mL^{-1} PA and 1 mg mL^{-1} S-PANI ink phase was placed into contact with 1 mg mL^{-1} POSS-NH_2 and allowed to assemble for 2 minutes prior to reducing the volume at 2 μL s^{-1}, and indicated the apparent surface coverage was 86%.

To gain further insights into the interfacial morphological features of films collected from the interface, scanning electron microscopy (SEM) and atomic force microscopy (AFM) were used, as illustrated in Figs. 2c and S4 respectively. The interfacial assembly was transferred to a silicon wafer from a pristine PA/S-PANI – POSS-NH_2 interface, generated by exchanging the ink phase for pure water and matrix phase for pure silicone oil. Fig. S4 shows the height profile of the interfacial film to have an average thickness of ~ 240 nm and a roughness of 30 nm in the middle of the film. Fig. 2c shows the analogous SEM image of the film, showing the roughness of the interface and shape of the dried S-PANI particles. Additional SEM images from PA/S-PANI collected from the interface with six different PA concentrations are provided in Fig. S5, and offer additional support for the increased size of the doped PS/S-PANI determined by the DLS measurements in Fig. 1b. Fig. S5 also shows that the morphology of the films change as a function of PA concentration since voids are observed in films with low PA content and the PA/S-PANI complexes are much less overlapped. This might imply different percolation paths for the current flow between the electrodes. It is also possible that higher concentrations of PA promote thicker films in-situ where the outermost PA/S-PANI complexes near the interface are weakly bound to the interface. We would expect that this increase in thickness correlates with an increase in

conductance since this would improve the PA/S-PANI overlap and increase the number of percolation pathways further.

2.3 Electrical Properties of PA/S-PANI Interfacial Assembly

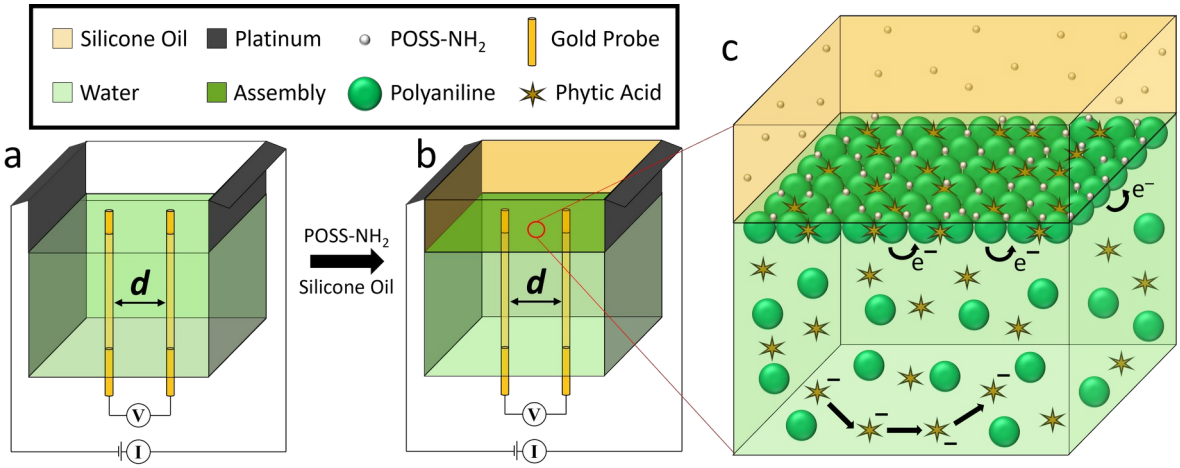

Figure 3: Schematic diagram of electrical measurement of jammed interface. (a) Four-point probe configuration of electrical measurement with current applied between platinum plates and voltage measured between gold probes (no oil phase). (b) Four-point probe configuration as POSS-NH_2 ligand solution is placed atop the PA/S-PANI solution to form jammed interface. (c) Schematic of the conductive mechanisms in the system: in solution (ionic conductivity) and along interface (electronic conductivity).

The arrangement of NPSs at the interface dictates the electrical conductivity, since efficient in-plane charge transport depends on the intimate overlap of S-PANI complexes with no insulating silicone oil in between. The jammed nature of the interface ensures this requirement, but how densely packed the interfacial layer is can significantly influence the rearrangement process and affect the overall conductivity. Fig. 3 shows a schematic of the four-point probe measurement used to characterize the electrical properties of the jammed PA/S-PANI interface between the ink phase (1 mg mL^{-1} S-PANI and controlled between 0.01–2 mg mL^{-1} PA) and the matrix phase (5 cSt silicone oil with 1 mg mL^{-1} POSS-NH_2). Fig. 3a shows the experimental schematic for the conductance measurements using a customized polylactic acid (PLA) cell where two platinum electrodes were placed at opposite cell edges and 1 mm diameter gold wires were precisely placed 1 cm from the edge. This generated a 1 cm separation distance *d* between the middle gold probes. In typical experiments, a 40 μA DC

current was applied to the platinum electrodes, and voltages between 0.5 x 10^{-3}–1.5 V were measured between the gold probes.

Bulk solution measurements on the ink phase were conducted by dispensing 10 mL of the ink phase with PA concentrations ranging between 0–2 mg mL^{-1}, and three S-PANI concentrations (0.1-, 1-, and 10 mg mL^{-1}) to assess the base line conductance with no interface. Here, the measured resistance of the ink solutions between the gold probes decreased exponentially with the concentration of the charged species given the greater number of charged entities increased the number of ions in solution. The total resistance was calculated by multiplying the resistance value measured (*V*/*I*) by the ratio of the length of the cell (3 cm) to the distance between the probes (1 cm) as well as the ratio of the width of the cell (3cm) to the length of the cell (3cm). The resistance of the S-PANI solution series decreased from 80 kΩ to 2.5 kΩ (Fig. S6a), while the conductance, calculated by the reciprocal of the resistance, increased from 0.013 mS to 0.385 mS (Fig. S6b). Figs. S7 and S8 show the same characterizations, but for varying the PA concentration (Fig. S7) and combined PA/S-PANI combined ink phase (Fig. S8, 1 mg mL^{-1} S-PANI with the different PA concentrations). Notably, the resistance of these bulk solutions remain stable with increasing measurement time, indicative of ionic conductivity. The bulk solution conductance for these samples also shows the increasing trend persists, where the concentration of charge carriers (PA, S-PANI, and PA/S-PNAI aggregates) positively correlates with the overall conductance. In the case of PA/S-PANI inks, the conductance increased from 0.07 mS for 0.01 mg mL^{-1} PA with S-PANI to 6.85 mS for 2 mg mL^{-1} PA with S-PANI.

With the baseline bulk solution conductivity addressed, any change to the conductance of the systems when the POSS-NH_2 silicone oil solution is added on top of the PA/S-PANI solution (Fig. 3b) must be attributed to the generation of the densely packed interface and excess PA/S-PANI complexes near the interface. Here, in-plane electrical conductivity of the

conductivity, while ionic conductivity is prevalent in the bulk ink phase. Once the ligand is gently placed atop the ink phase, the electrical measurements were performed in a similar manner as the bulk solution measurements were conducted, making sure the gold electrodes pierce the interface (see Methods), to elucidate the extent to which the interfacial film contributes to the conductance of the system.

Fig. 4a shows conductance measurements for PA/S-PANI inks as a function of time as the interface is equilibrated when the POSS-NH_2 silicone oil solution is placed on top after ~180 s. It is immediately apparent that the interface contribution to the conductivity is much larger for higher PA concentrations. This can be seen in Fig. 4a where the solid red line represents the conductance for the 2 mg mL^{-1} PA and 1 mg mL^{-1} S-PANI when no interface is present, reaching 6.85 mS, but when the interface is present (dashed red line), the conductance increases dramatically to 93 mS, representing a 13.5 x increase. Using lower PA concentrations, the increase in conductance is much less; even modest PA concentrations, for example 0.5 mg mL^{-1} PA, only increases the conductance by 0.58 mS. Fig. 4b summarizes the equilibrium conductance values after 600 s using only PA (red), bulk solution PA/S-PANI inks (blue), and PA/S-PANI inks with interfaces present (black). These data show that the addition of the PA/S-PANI inks increase the conductance much more when an interface is present, suggesting the introduction of the ligand establishes new conductive pathways at the interface. These new pathways likely facilitate charge transport in the plane of the interface since the

POSS-NH_2 in the bulk oil phase is unprotonated, and there was no addition of ions in the bulk ink phase. Electron transport through interconnected, percolated pathways from the overlap of PA/S-PANI complexes at the interface and/or charge transport due to double layer effects at and near the interface are likely contributing factors to the increase in conductance. Moreover, the majority of the conductance stems from the sheet conductance (mS $sq.^{-1}$) of the interfacial film, calculated as the total conductance of the system and subtracting the bulk solution contributions, which is plotted in Fig. 4c. These findings carry intriguing implications for 3D printed all liquid electronics since there are enhanced electrical characteristics, given by the densely packed interface, and has significant advantages in reconfigurability, given by the light weight and fluid nature of the printed center. For example long liquid wire threads can be printed using optimal printing conditions (i.e., ink flow rate, print speed, matrix viscosity, component concentrations, etc.).

2.4 Electrical Properties of PA/S-PANI All-Liquid Wires

To demonstrate the ability to print conductive, all-liquid wires, we developed a custom printing cell made from PLA. The bottom of the cell features strategically positioned wells where PA/S-PANI ink droplets were placed prior to filling the container with the ligand solution, ensuring robust contact with the gold probes placed in the wells (Fig S9). Next, a uniform tubular wire is 3D printed between the electrodes using an INKREDIBLE+ 3D printer from Cellink. The printability of the wire structures was a function of the IFT reduction (rate of PA/S-PANI assembly at the interface, which depends on NPS component concentrations), printing flow rate, and matrix phase viscosity, all of which are factors that can suppress Plateau-Rayleigh instabilities. Fig S10a qualitatively shows that low matrix phase viscosity (i.e., 5–20 cSt, Fig S10b and S10c) could be printed likely due to fast POSS-NH_2 diffusion to the interface, while high matrix viscosity (i.e., >1000 cSt, Fig S10f and S10g) was

beneficial due to the increased inertial forces, which gave highly concentrated POSS-NH_2 solutions enough time to diffuse to and stabilize the interface. Matrix phases with moderate viscosities (i.e., ~100–1000 cSt, Fig S10d and S10e) were difficult to print since the decrease in POSS-NH_2 diffusion was not offset enough by the resistance to deformation caused by increasing the viscosity. However, high matrix phase viscosity also limits the reconfigurability of the printed structures as more work would be needed to move the liquid structures though the viscous media. Here, the optimal printing conditions were found to be printing with a 22-gauge needle with a 0.14 mL s^{-1} volumetric flowrate in 20 cSt silicone oil that was supersaturated with POSS-NH_2. While we acknowledge that the low viscosity of the matrix phase used here may problematic for very large mechanical perturbations, which could cause the liquid wires to deviate from their straight path or even break, we did not encounter any damage to our wires over the course of our experimentation. The diameter of the liquid wires could tuned by slightly modifying these printing conditions in addition to the print head speed. For all printing applications, 2 mg mL^{-1} PA and 1 mg mL^{-1} S-PANI ink solutions were used as these solutions were stable over long periods of time and produced the best electrical properties. More detailed information regarding the printing setup can be found in the supporting information (see 3D Printing of All-Liquid PA/S-PANI Wires: Techniques and Settings).

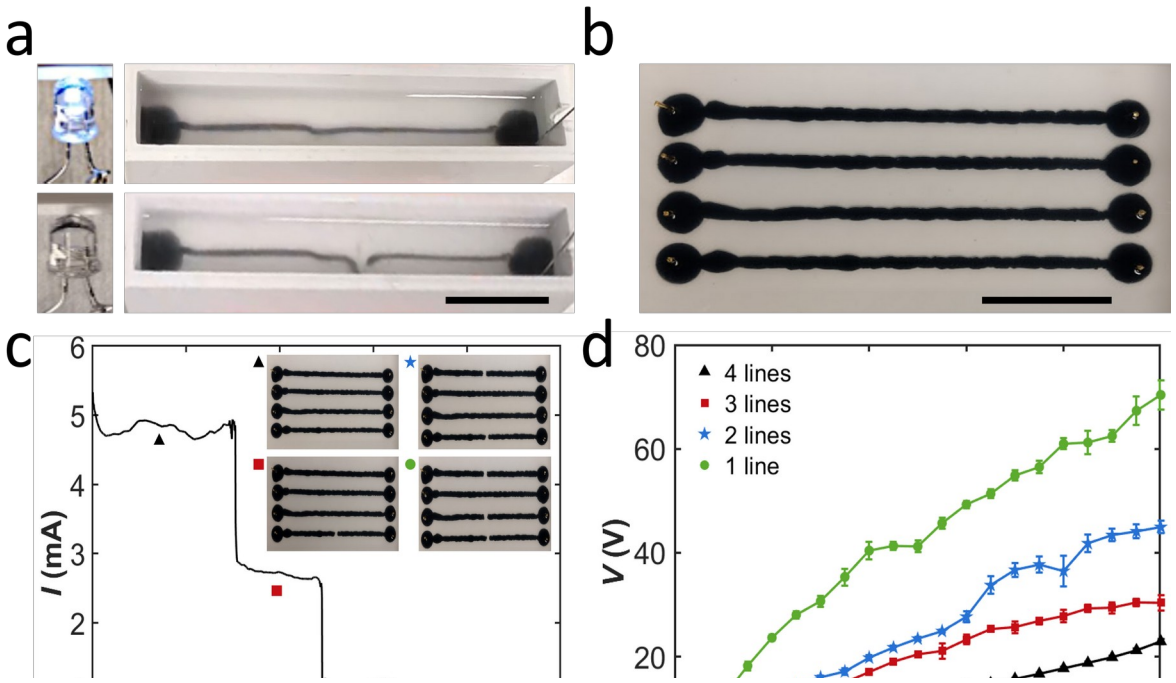

The structural integrity and electrical functionality of the printed tubular wires were exceptional, as shown in Figure 5a. These wires were capable of consistently completing a series circuit, demonstrated by the successful lighting of an LED. This integrity was further tested by intentionally severing the wires, which predictably interrupted the circuit and extinguished the LED, validating the all-liquid wire's conductive path. The dynamic electrical behavior of the wire during in-situ printing was captured in Figure S11, where there is no current until the tubular prints connected the electrodes (~ 360 s), establishing a conductive pathway such that a current of approximately 0.25 mA was achieved using a 30 V DC bias. After establishing the connective pathway, the current continually increased to 0.38 mA after 800 s, indicating the progressive ordering and better packing of the PA/S-PANI at the interface which allowed the jammed structure to support more efficient electron flow. These values

suggest a ~78.9 kΩ resistance, a value much higher than previously determined by the four-point probe measurement using the same PA/S-PANI concentrations. The nature of the jammed interface precluded the use of a four-point probe setup, which would have necessitated additional probe insertions that could disrupt print connectivity. Since the printing setup used a two-probe geometry and had a much greater distance between the gold probes, contact resistance at the probes, total interfacial surface area, dielectric loss as heat, and intermittent areas of high resistance from poorer ordering likely account for the increased resistance in this printing geometry. We also note that water decomposition could lead to the occasional formation of bubbles if the circuit is in use with moderately high voltages for a prolonged amount of time. Using a similar printing cell, but employing a rotating extruder (Fig. S12a), enabled precise control of the wire's placement and 3D geometry, including the versatility in producing complex structures, such as helices (Fig. S12b). Electrical measurements indicated that coiled structures were electrically connected, however, the difference in density caused the structure to eventually collapse.

Further experiments involved printing parallel circuits composed of multiple PA/S-PANI wires, as illustrated in Figures 5b–c, with the device set up depicted in Fig S13a. These wire circuits were constructed by the subsequent extrusion of four wires connected in parallel, where disconnection of a single wire through mechanical cleavage resulted in the cessation of current through that branch, but continued in all other branches that were still connected. This independence in current control for each wire was critical for demonstrating the modularity of our system. Fig. 5c shows the *in-situ* operation of a parallel circuit configuration using a 50 V source, and shows that highest current, 4.9 mA when four wires were connected, was reduced upon sequential scission of corresponding wires. Upon sequentially disconnecting the wires, currents of 4.9, 2.71, 1.17, 0.71, and 0 mA were recorded in descending number of wires from four to zero. Once three wires were cut, leaving a single current carrying wire, effectively

converted the parallel configuration back to a series one. Following scission of the last wire, all the electrical pathways were severed, and no current flowed as evidenced in Supplementary Movie 1 (SM1) where an LED is turned off.

Another necessary measurement to conduct in the parallel configuration is applying a constant current and measuring the necessary voltage to achieve the current with a different number of wires, and as a function of time (Fig. S14a–b), as shown in Fig 5d for current ranging from 10–1000 μA. By reducing the number of available current pathways, the corresponding driving force (voltage) needed to be increased to achieve the current as Fig. 5d demonstrates. These measurements underscore the increase in equivalent resistance (R_{eq}) from 16.5 kΩ to 69.9 kΩ, which were calculated from the slope of the linear portion of the plot between 100 to 600 μA, as the number of wires was reduced from four to one. In classic parallel circuits, the expected equivalent resistance can be determined from the summation of the inverse resistances ($1/R_{eq} = \Sigma\ 1/R_i$). By taking the resistance of one wire to be 69.9 kΩ, we recover a R_{eq} value of 17.47 kΩ using four wires with the same resistance. We measured a R_{eq} of 16.5 kΩ using four wires, which is very close to the expected 17.47 kΩ, and further highlights the uniform nature of the printed constructs. Despite the increase in contact resistance, the 3D printing of all liquid wires demonstrates the modularity of our system and the ability to arbitrarily choose the number, position, and length of the wires.

2.5 Reconfigurability of PA/S-PANI All- Liquid Wires

A unique characteristic of the PA/S-PANI liquid wire is the innate capacity for self-reconfigurability after the wire has been mechanically broken, a stark contrast to the permanent damage typical of traditional solid-state electronics, and has been little explored in the context of 3D printed liquid wires. Due to the intrinsic charge carrying character and malleable liquid core, the application of voltage leads to a buildup of charge at the ends of the

broken wire. Once enough charge is built such that electrostatic forces overcome the drag forces, the wires attain the ability to repair their conductive pathway by electrocoalescence, a significant advancement in the field of flexible and adaptive electronics. It should be noted that wire geometry and the magnitude of the applied bias greatly affect what the maximum distance between the ends of the wire can be to still achieve the reconfigurability effect. These liquid wires can be repaired in two ways; one by introducing additional PA/S-PANI ink in between the broken ends of the severed site as shown in Fig. 6a at relatively lower voltages (V ~150 V), and another whereupon no additional material is added, but the voltage required grows to ~450 V. Since the voltage being applied is bipolar, the ends build up opposite charges, which effectively polarize a droplet introduced in between the broken ends. If an ink droplet is placed within ~3–4 mm, this effect also drags the droplet to the correct location where the breakage occurred. If the voltage is sufficiently high, the droplet will deform slightly to accommodate the electrostatic interactions, bringing the droplet and each end of the broken wire into intimate contact with one another. At this stage, it is likely that the PA/S-PANI complexes at the interface of the additional ink droplet is not yet fully jammed or in a very dense packing since the droplet is freshly made. The close contact and less jammed packing can lead to a coalescence as detailed in Figure 6a. This initiates a self-assembly process at the interface, effectively mending the break and restoring the conductive jammed interface. This reconfigurability mechanism mitigates the interfacial tension between the newly added ink phase and the matrix phase, reinstating electrical conductivity. It should be noted that coalesce across the printed structure is not strictly necessary to restore the current; only the shells of the jammed ink phases need to be in contact. However, if the ink phases do coalesce, it improves the mechanical robustness to later fracture. The supplementary movie SM2 provides a detailed visualization of this reconfiguration process in the reconnection of all four wires using a 210 V source.

We further explored the wire's self-reconfigurability under electrical field in a parallel circuit by applying a controlled voltage thorough the circuit and measured the current *in-situ*. The application of voltage was kept constant at 210 V and every time a wire was reconnected a corresponding increase in the current was observed, increasing in order: 0, 5.2, 9.1, 15.3, and 24.1 mA (Fig. S15), indicating a current carrying pathway was reconnected. After reconnecting all four branches in the parallel circuit and reducing V to 50 V (at ~85 s) a value of 4.7 mA was recovered, which is roughly the same value as the pristine four wire parallel circuit. This suggests that the reconnection is robust and generates a similar amount of charge

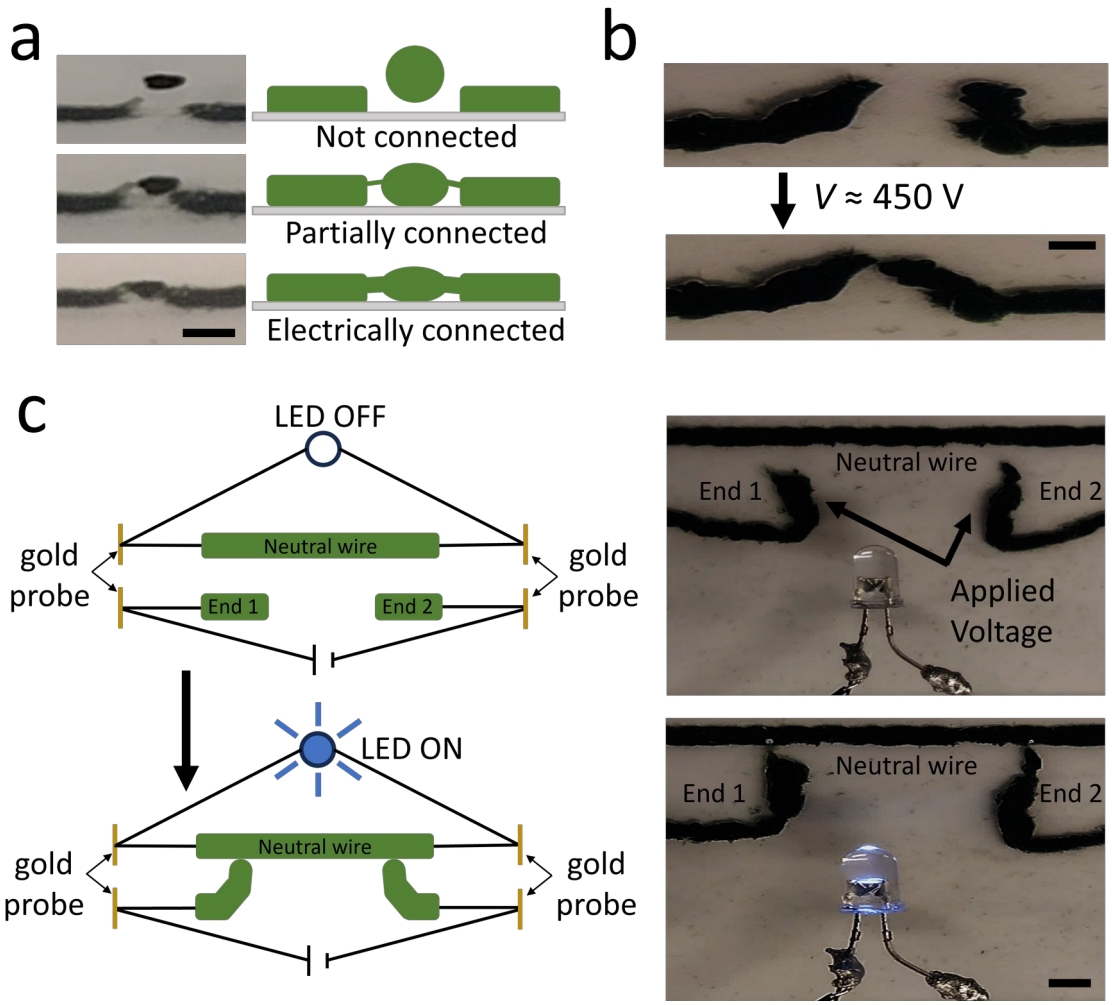

Figure 6: Schematic of reconfigurability and re-connectivity of PA/S-PANI liquid wires. (a) Reconnection of a cleaved wire with additional PA/S-PANI droplet placed in between the cleaved ends. Scale bar is 6 mm. (b) Self-reconnection of cleaved wire without additional ink solution at a constant voltage of 450 V and 7 mm spacing. Scale bar is 5 mm. (c) Schematic of using liquid wires to recircuit two individual circuits with wire ends for successful current flow through the liquid wire to light an LED. Scale bar is 6 mm.

carrying capacity despite the fact the area around the reconnection may be much smaller than the original tubular wire.

Instead of adding additional ink material to promote reconnection between two severed ends of a PA/S-PANI wire, a similar result can be achieved by using a larger applied voltage and no additional ink. Here a large electric field is generated between the ends of the broken wire which can be visualized by the repetitive cycling movement of an ink phase microdroplet between the broken ends of the wire (typically observed when above an applied voltage of ~300 V), denoting charge transfer from one contact to the other, as exhibited in SM3. The precise mechanism for this charge storage and transport is currently under study to more fully understand what morphological aspects of the densely packed PA/S-PANI interface is contributing to the charge/electron transport. This motion persists above ~350 V, but once the voltage surpasses ~400 V the ends of the wires can come together and the same self-assembly process at the broken area facilitates the reconnection as seen in Fig. 6b and SM4 and SM5. We note, however, that excessively high voltages ($\geq$ 800 V) were found to be detrimental, leading to the boiling of the water in the ink phase rather than aiding in the healing process, as seen in SM6.

The remarkable reconfigurability of the PA/S-PANI all-liquid wire is further highlighted within a repairable electrical circuit context. As illustrated in Figure 6c, an open circuit created by deliberately severing the bottom wire undergoes a fascinating transformation upon the application of voltage. If a neutral wire that is not connected to any voltage source is positioned closer to the ends of the wire than they are to each other, the wires can actually polarize the neutral wire. If the wire ends are placed at a distance equivalent to or less than distance between the neutral wire and the broken ends, the reconfigurability process will procced normally, as if the neutral wire was not present. This stimulus instigates charge transfer along the cleaved ends of the wire, driving the spontaneous

formation of a completed circuit. The re-illumination of the previously inactive LED serves as a visual testament to the ability of the wire to not only reconnect but also to fully restore its conductive properties, as documented in Supplementary video SM7 and Fig 6c (bottom). As seen in SM7 the small microdroplet between the neutral wire and broken wire again shows the cyclic charge transfer until the charge is built up enough to force the ends of the wire to come into contact with the previously neutral wire, completing the circuit. Amazingly, the small area of wire contact is sufficient to establish electrical transport and is remarkable because the interface, as established from the AFM measurements, is only ~ 240 nm thick. Nevertheless, the self-sufficient healing mechanism demonstrated here underscores the innovative design of all-liquid wires and has great potential for integration into functional electronic systems and their suitability for a new generation of adaptive liquid electronics.

3. Conclusion

In conclusion, PA/S-PANI all-liquid electronics demonstrate good fundamental electrical properties and stability, but also the ability to print tubular wires in arbitrary shapes and circuits. These attributes are a result of the synergistic effects of the PA/S-PANI complex decreasing the IFT of the ink–matrix interface, which allows for the suppression of the Plateau-Rayleigh instabilities, and enhancing the inherent conductivity of the interfacial films from the dense packing and overlap of conductive moieties at the interface. Furthermore, the unique ability of the 3D printed PA/S-PANI wires to reconfigure under an applied voltage through the disconnected ends of a broken wire represents a pivotal shift in the landscape of all-liquid electronic materials. Our experiments have successfully shown that these wires can restore their conductive pathways after being severed and achieve charge-carrying capacity very close to that of a pristine wire, likely because the majority of the conductivity originates from the interface. We demonstrated that the application of voltage can also alter the circuit

setup to turn on an LED, an intriguing step toward developing autonomous circuits which can switch the number of resistive elements and repair previously broken circuits on demand. The potential for these materials extends into myriad domains, including wearable technology, bioelectronics, and flexible electronics, where resilience and adaptability are crucial. As the demand for sustainable and versatile electronic components grows, the development of all-liquid wires is positioned to meet these needs and pave the way for the next generation of electronic devices.

4. Experimental Section/Methods

Materials and Solution Preparation:

Synthesis of Phytic Acid Doped Sulfonated Polyaniline Solution - Ink Phase

Polyaniline (PANI) was synthesized via an oxidative polymerization process developed by MacDiarmid et al. [41] and adapted by Wei et al. [40] and Farrokhzad et al. [51] Initially hydrochloric acid (37% Sigma–Aldrich, 14.78 mL) and aniline monomer (Sigma–Aldrich, 16.76 g) were dissolved in deionized water (600 mL) and the solution was stirred vigorously in an ice bath maintained at 5°C in a 1 L flask. After 30 minutes of stirring, the polymerization reaction was initiated with ammonium persulfate (Sigma–Aldrich, 0.18 mol in 60 mL deionized water), which was gradually added into the flask over 30 minutes. The reaction mixture was then stirred for 3 hours at 5°C. The resulting emeraldine salt precipitate was filtered and washed thoroughly with deionized water and methanol. To convert the emeraldine salt to the emeraldine base, ammonium hydroxide (Sigma–Aldrich, 1 M) was stirred into the filtered solution at room temperature. The product was filtered and dried under vacuum in an oven at 60°C overnight, yielding a blue powder.

The PANI was sulfonated by a method developed previously by Wei et al. [40] Briefly, for every 0.5 g of dried emeraldine base, 2.5 mL of phenylhydrazine (Sigma–Aldrich) was added and mixed in a glass mortar. The mixture was pressed with a glass pestle for 10 minutes and subsequently stirred for one hour to complete the reducing reaction, before being diluted with ethyl ether (Sigma–Aldrich, 75 mL). The product (leucoemeraldine base) was filtered and washed with ethyl ether, then suction dried. The sulfonation reaction was carried out using precooled (5 °C) fuming sulfuric acid (Sigma–Aldrich, 10 mL), which was added to the dried leucoemeraldine base in the mortar and stirred for 1 hour in an ice bath. The reaction was terminated by slow addition of the sulfonated PANI (S-PANI) into ice water, which precipitated the S-PANI polymer. The S-PANI precipitates were cleaned and filtered on a

vacuum funnel, after which the filter cake was dispersed at a high concentration in water. Subsequently, dialysis was performed for 1 week using a Snakeskin dialysis tubing MWCO 5,000 (Thermo Fischer Scientific) while changing water two times a day to remove impurities. Following dialysis the concentrated S-PANI solution was diluted to 10 mg mL^{-1} in distilled water and stored at room temperature.

For all four probe conductivity experiments and printing, different phytic acid (PA, Sigma-Aldrich 50% wt.%) concentrations were added to the S-PANI to obtain the PA-doped S-PANI such that the final PA concentrations were controlled between 0.01–4 mg mL^{-1}. Above ~ 4 mg mL^{-1} PA the S-PANI and PA formed large colloidal aggregates that fell out of solution, so this value was used as the maximum for any doped S-PANI/PA solutions. While increasing the concentration of PA can enhance conductivity, the aggregation could adversely affect the interface stabilization in 3D prints as well as the performance of the material over long periods of time. Prior to any measurement, the S-PANI/PA solutions were made fresh and vortex mixed for 2 minutes.

Preparation of POSS-NH2 in Silicone Oil - Matrix Phase

The matrix phase was composed of silicone oil (Sigma-Aldrich), toluene (Sigma-Aldrich) and 3-[(2-aminoethyl)amino]propyl]-heptaisobutyl substituted polyhedral oligomeric silsesquioxanes (POSS-NH2, Sigma-Aldrich). Seven different viscosities of silicone oil were tested (5-, 20-, 100-, 500-, 1,000-, 5,000-, and 30,000 cSt), although only 5-, 20-, and 30,000 cSt silicone oils were routinely used since these viscosities produced the best printing results. For each viscosity a stock solution of highly concentrated POSS-NH_2, was fully solubilized with 10 mL toluene and then added to 300 mL silicone oil such that the final stock solution contained ~8 mg mL^{-1}. For tensiometry and four probe conductivity measurements, this stock solution was diluted to 1 mg mL^{-1}, and here only 5 cSt oil solutions were used. For printing

experiments, all silicone oil viscosities were tested using a 4 mg mL^{-1} POSS-NH_2 concentration.

Characterization:

FTIR:

1 mL of aqueous S-PANI polymer was deposited on a silicon wafer (CKplas) such that a thick film formed after the water was evaporated under ambient conditions. FTIR spectrometry was conducted by placing the collected polymer flakes on the diamond/ZnSe crystal of a Nicolet iS50 FT-IR from Thermo Scientific, and performing 64 scans in attenuated total reflectance (ATR) mode between 4000-400 cm^{-1}. The profile confirms sulfonation of the polymer.

DLS and Bulk Solution Conductivity Measurements:

Dynamic light scattering measurements were performed to determine the effect of PA concentration on the size of the S-PANI in solution using a Malvern Zetasizer Nano ZS instrument. 1 mL of diluted 1 mg mL^{-1} of the S-PANI solution was loaded into a disposable capillary cell and into the Zetasizer instrument, and backscatter measurements were performed (= 173°, = 25℃) following a thermal equilibration for ~ 1 minute. Signal intensity was collected over a period of 30 seconds to capture the autocorrelation function and averaged over three measurements. The average auto-correlation function was fit using CONTIN fitting methods to yield an average size, a polydispersity index, and a size distribution for each PA doped S-PANI bulk solutions.

The Zetasizer was also used to perform solution conductivity measurements using the Malvern DTS1070 disposable capillary cell. The conductivity measurements were taken using the same concentrations as the DLS measurements and were performed three times and averaged over 30 seconds.

Tensiometry:

A Krüss DSA30 pendant drop tensiometer was used for measuring the interfacial tension (IFT, γ) between water and silicone oil with independent measurements run for different ink phase and oil phase constituents and concentrations. The IFT was measured as a

function of time after injecting an aqueous droplet (~8–30 μL depending on the system constituents) into the oil phase, for 300 s, generally enough time to reach the saturated interfacial tension value and plateau. Aqueous solutions of PA, S-PANI, and PA doped S-PANI were prepared such that the S-PANI concentration was kept constant at 1 mg mL^{-1} S-PANI and used a constant POSS-NH_2 concentration of 1 mg mL^{-1}. γ was measured as a function of time by fitting the curvature of the droplet to the Young–Laplace equation and was collected at one frame per second. The aqueous phases were injected using a blunt needle with 1.21 mm.

SEM:

Scanning electron microscopy (SEM) was conducted using a Zeiss ULTRA 55–FESEM and 5 kV accelerating voltage to collect images of the dried films. SEM samples were prepared on air-plasma treated silicon wafers using a Harrick Plasma PDC-001 plasma cleaner. Samples were collected from the interface of bilayer layer systems with controlled amount of PA after carefully exchanging both the ink and matrix phases with pure water and oil. Additionally, a printed construct was also imaged using the optimum printing conditions.

AFM:

The PA/S-PANI layers were visualized using an Oxford Asylum Cypher scanning probe microscope in tapping mode with a Tap150Al-G cantilever (Budget Sensors) with a resonance frequency of 150 kHz and force constant of 5 N m^{-1}. AFM samples were prepared on air-plasma treated silicon wafers using a Harrick Plasma PDC-001 plasma cleaner and the PA/S-PANI layers were collected in the same manner as in the SEM sample preparation. Following image acquisition, surface roughness and layer thickness feature dimensions were determined following post-processing steps to remove the background slope.

Measurement of Conductivity and Electrochemical Properties of Planar Interfaces

The resistance and conductance of planar interfaces comprised using the conditions of the PANI printed liquid wires was measured using a four-probe measurement setup using a Keithly 2400 Source meter. A custom made 3 cm × 3 cm × 3 cm polylactic acid (PLA) cell was 3D printed such that platinum sheets (Thermo Scientific, 0.25 mm thickness, 99.9%) cut to the proper dimensions could be placed at the edge of the cube. Two small holes were drilled in the PLA cube base so that gold wires (Beantown Chemical, 1mm diameter, 99.95%), cut to

2.5 cm in length, were precisely placed 1 cm from the edges of the cube such that the distance between the gold was 1 cm and were protruding ~ 1.5 cm from the base. Controlled current (typically ~ 40–60 μA) was applied to platinum electrodes, while the voltage was measured between the gold probes. Measurements on the ink phase were conducted by dispensing 10 mL of the ink phase with PA concentrations ranging between 0–2 mg mL^{-1} and three S-PANI concentrations (0.1-, 1-, and 10 mg mL^{-1}) to assess the base line conductance of the bulk solution with no interface. Measurements were typically collected for ~10 minutes, although there was no change in the conductance after 5 minutes. Interfacial conductance measurements were conducted in the same way expect the POSS-NH_2 solution in 5 cSt oil was placed on top of the ink phase after 200 s, after which a marked decrease in the resistance was noted. A detailed schematic is provided in the SI to further illustrate this experimental setup.

3D Printing of All-Liquid PA/S-PANI Wires: Techniques and Settings

Two custom 3D-printed PLA cells were made for the printing of the PA/S-PANI wires, one with the dimensions 12.5 cm × 2 cm × 2.5 cm for single wire prints and one with 13 cm × 8 cm × 2.5 cm dimensions to print multiple wires in one cell. These cells were designed such that gold probes were placed 1 cm from the edge and were protruding ~ 1.5 cm from the base, similar to the planar cell. However, 3 mm wells were inserted into the area where the gold probes protrude so that the aqueous ink phase could be placed there prior to any silicon oil introduction. Placing the ink phase in contact with the gold probes prior to the silicon oil is very important as to have intimate contact between the water and gold probes without insulating silicone oil in between, which would significantly increase the contact resistance. After placing the POSS-NH_2 silicone oil solution on top of the aqueous ink filled well, the cell was loaded into an INKREDIBLE+ 3D printer (Cellink) 3D-printed, with the print heads replaced by a 22-gauge blunt, stainless steel needle that was flow controlled by controlling the input pressure and the 3D printed software. The trajectory for the print head was generated using a G-code script which could be used to control the spatial location of the start and end point of the line as well as the print speed. Several printing speeds, flow rates, and needle diameters were tested, although the best results typically occurred with a print speed of 1.9 mm s^{-1}, a flow pressure of ~1.5 psi, and a 22-gauge blunt needle. Before printing, the gold probes in the cell were carefully attached to the electrodes so that conductivity measurements could be collected in-situ. Fresh Silicone oil was prepared and vortex mixed for 3 minutes prior to use. Moderate silicone oil viscosities (e.g., 100–1000 cSt) produced nonuniform prints

due to insufficient suppression of the Plateau-Rayleigh instability from slow diffusion of POSS-NH_2 to the interface and the quick return to spherical like defects in the printed structure.

When using the cell for multiple PA/S-PANI prints, the gold probes were connected in parallel using standard 24-gauge AWG wires (Jonard Tools) such that each printed wire acted as a resistor in parallel with each other. An LED (3 V) was placed across the wires as a visual indicator that current was passing through the system. If all the wires were cut, the LED turned off and confirmed no current could be passed through the system. Using this two-probe setup, either the current or voltage could be controlled using the Keilthy 2400 Source meter up to 210 V and 1 A, and could be done as a function of the number of S-PANI printed constructs and time. To apply higher voltages (up to 5 kV), a 20459 Hamburg source from 3B Scientific GmbH was used in the printing reconfiguration experiments.

3D Printing an All-Liquid S-PANI Coiled Wire

To print 3D PA/S-PANI constructs in a coil geometry an Ultimaker S3 printer was used in conjunction with a homemade rotating rod such that a syringe could be attached to the rod and that the speed could be controlled by a motor. By controlling the printing conditions (print speed, flow rate, and nozzle diameter, etc.), using the highest viscosity silicone oil (30,000 cSt), and controlling the motor speed, we could define the specific dimensions of the liquid wire (i.e., number of turns, length, etc.). Our modified 3D printer was utilized to fabricate an all-liquid coiled structure. A schematic is provided in the SI to further illustrate this experimental setup.

Acknowledgements

ZF, PYK, and JH contributed equally to this manuscript. This work supported by the U.S. Department of Energy, Office of Science, Office of Basic Energy Sciences, Materials Sciences and Engineering Division under Contract No. DE-AC02-05-CH11231 within the Adaptive Interfacial Assemblies Towards Structuring Liquids program (KCTR16). Dynamic light scattering and scanning electron microscopy measurements conducted at the Molecular Foundry was supported by the Office of Science, Office of Basic Energy Sciences, of the U.S. Department of Energy under Contract No. DE-AC02-05CH11231 and is gratefully acknowledged by TPR. We also acknowledge Guanhua Fu and the Jacobs Institute for Design

Innovation for the use of the advanced prototyping lab in helping to print the PLA cells used in this work.

Received: ((will be filled in by the editorial staff))

Revised: ((will be filled in by the editorial staff))

Published online: ((will be filled in by the editorial staff))

References:

[1] Park, Y. G.; Yun, I.; Chung, W. G.; Park, W.; Lee, D. H.; Park, J. U. High-Resolution 3d Printing for Electronics. *Adv. Sci.* **2022**, 9, DOI: 10.1002/advs.202104623.

[2] Rao, C. H.; Avinash, K.; Varaprasad, B. K. S. V. L.; Goel, S. A Review on Printed Electronics with Digital 3d Printing: Fabrication Techniques, Materials, Challenges and Future Opportunities. *J. Electron Mater.* **2022**, 51, 2747-2765, DOI: 10.1007/s11664-022-09579-7.

[3] Wiklund, J.; Karakoç, A.; Palko, T.; Yigitler, H.; Ruttik, K.; Jäntti, R.; Paltakari, J. A Review on Printed Electronics: Fabrication Methods, Inks, Substrates, Applications and Environmental Impacts. *J. Manuf. Mater. Proc.* **2021**, 5, DOI: 10.3390/jmmp5030089.

[4] Popple, D.; Shekhirev, M.; Dai, C. H.; Kim, P.; Wang, K. X.; Ashby, P.; Helms, B. A.; Gogotsi, Y.; Russell, T. P.; Zettl, A. All-Liquid Reconfigurable Electronics Using Jammed Mxene Interfaces. *Adv. Mater.* **2023**, DOI: 10.1002/adma.202208148.

[5] Han, X. T.; Xiao, G. C.; Wang, Y. C.; Chen, X. N.; Duan, G. G.; Wu, Y. Z.; Gong, X.; Wang, H. X. Design and Fabrication of Conductive Polymer Hydrogels and Their Applications in Flexible Supercapacitors. *J. Mater. Chem. A* **2020**, 8, 23059-23095, DOI: 10.1039/d0ta07468c.

[6] Peng, Q. Y.; Chen, J. S.; Wang, T.; Peng, X. W.; Liu, J. F.; Wang, X. G.; Wang, J. M.; Zeng, H. B. Recent Advances in Designing Conductive Hydrogels for Flexible Electronics. *Infomat* **2020**, 2, 843-865, DOI: 10.1002/inf2.12113.

[7] Shin, S.; Hyun, J. Matrix-Assisted Polymerization of a 3d Conductive Hydrogel Structure. *ACS Appl. Mater. Interfaces* **2022**, 14, 52516-52523, DOI: 10.1021/acsami.2c15603.

[8] Xie, X. J.; Xu, Z. G.; Yu, X.; Jiang, H.; Li, H. J.; Feng, W. Q. Liquid-in-Liquid Printing of 3d and Mechanically Tunable Conductive Hydrogels. *Nat. Commun.* **2023**, 14, DOI: 10.1038/s41467-023-40004-7.

[9] Kim, M. S.; Kim, S.; Choi, J.; Kim, S.; Han, C.; Lee, Y.; Jung, Y.; Park, J.; Oh, S.; Bae, B. S.; Lim, H.; Park, I. Stretchable Printed Circuit Board Based on Leak-Free Liquid Metal Interconnection and Local Strain Control. *ACS Appl. Mater. Interfaces* **2022**, 14, 1826-1837, DOI: 10.1021/acsami.1c16177.

[10] Li, G. Q.; Zhang, M. Y.; Liu, S. H.; Yuan, M.; Wu, J. J.; Yu, M.; Teng, L. J.; Xu, Z. W.; Guo, J. H.; Li, G. L.; Liu, Z.; Ma X. Three-Dimensional Flexible Electronics Using Solidified Liquid Metal with Regulated Plasticity. *Nat. Electron.* **2023**, 6, 154-163, DOI: 10.1038/s41928-022-00914-8.

[11] Li, G. Y.; Sun, F. K.; Chen, H. S.; Jin, Y.; Zhang, A. B.; Du, J. K. High-Efficiency Large-Area Printed Multilayer Liquid Metal Wires for Stretchable Biomedical Sensors with Recyclability. *ACS Appl. Mater. Interfaces* **2021**, 13, 56961-56971, DOI: 10.1021/acsami.1c17514.

[12] Neumann, T. V.; Dickey, M. D. Liquid Metal Direct Write and 3d Printing: A Review. *Adv. Mater. Technol.* **2020**, 5, DOI: 10.1002/admt.202000070.

[13] Teng, L.; Ye, S. C.; Handschuh-Wang, S.; Zhou, X. H.; Gan, T. S.; Zhou, X. C. Liquid Metal-Based Transient Circuits for Flexible and Recyclable Electronics. *Adv. Funct. Mater.* **2019**, 29, DOI: 10.1002/adfm.201808739.

[14] Gao, N. W.; He, Y. L.; Tao, X. L.; Xu, X. Q.; Wu, X.; Wang, Y. P. Crystal-Confined Freestanding Ionic Liquids for Reconfigurable and Repairable Electronics. *Nat. Commun.* **2019**, 10, DOI: 10.1038/s41467-019-08433-5.

[15] Li, X. G.; Liu, R.; Huang, M. R. Facile Synthesis and Highly Reactive Silver Ion Adsorption of Novel Microparticles of Sulfodiphenylamine and Diaminonaphthalene Copolymers. *Chem. Mater.* **2005**, 17, 5411-5419 10.1021/cm050813s.

[16] Tao, X. L.; Liao, S. L.; Wang, S. Q.; Wu, D.; Wang, Y. P. Body Compatible Thermometer Based on Green Electrolytes. *ACS Sensor*s **2018**, 3, 1338-1346, DOI: 10.1021/acssensors.8b00249.

[17] Silva, A. F.; Paisana, H.; Fernandes, T.; Góis, J.; Serra, A.; Coelho, J. F. J.; de Almeida, A. T.; Majidi, C.; Tavakoli, M. High Resolution Soft and Stretchable Circuits with Pva/Liquid-Metal Mediated Printing. *Adv. Mater. Technol.* **2020**, 5, DOI: 10.1002/admt.202000343.

[18] He, H.; Ouyang, J. Y. Enhancements in the Mechanical Stretchability and Thermoelectric Properties of Pedot:Pss for Flexible Electronics Applications. *Accounts Mater. Res.* **2020**, 1, 146-157, DOI: 10.1021/accountsmr.0c00021.

[19] Gannarapu, A.; Gozen, B. A. Freeze-Printing of Liquid Metal Alloys for Manufacturing of 3d, Conductive, and Flexible Networks. *Adv. Mater. Technol.* 2016, 1, DOI: 10.1002/admt. 201600047.

[20] Fantino, E.; Roppolo, I.; Zhang, D. X.; Xiao, J. F.; Chiappone, A.; Castellino, M.; Guo, Q. Q.; Pirri, C. F.; Yang, J. 3d Printing/Interfacial Polymerization Coupling for the Fabrication of Conductive Hydrogel. *Macromol. Mater. Eng.* **2018**, 303, DOI: 10.1002/mame.201700356.

[21] Shin, M.; Song, K. H.; Burrell, J. C.; Cullen, D. K.; Burdick, J. A. Injectable and Conductive Granular Hydrogels for 3d Printing and Electroactive Tissue Support. *Adv. Sci.* **2019**, 6, DOI: 10.1002/advs.201901229.

[22] Yuk, H.; Lu, B. Y.; Lin, S.; Qu, K.; Xu, J. K.; Luo, J. H.; Zhao, X. H. 3d Printing of Conducting Polymers. *Nat. Commun.* **2020**, 11, DOI: 10.1038/s41467-020-15316-7.

[23] Han, J. Q.; Ding, Q. Q.; Mei, C. T.; Wu, Q. L.; Yue, Y. Y.; Xu, X. W. An Intrinsically Self-Healing and Biocompatible Electroconductive Hydrogel Based on Nanostructured Nanocellulose-Polyaniline Complexes Embedded in a Viscoelastic Polymer Network Towards Flexible Conductors and Electrodes. *Electrochim. Acta* **2019**, 318, 660-672, DOI: 10.1016/j.electacta.2019.06.132.

[24] Wissman, J.; Dickey, M. D.; Majidi, C. Field-Controlled Electrical Switch with Liquid Metal. *Adv. Sci.* **2017**, 4, DOI: 10.1002/advs.201700169.

[25] Forth, J.; Kim, P. Y.; Xie, G. H.; Liu, X. B.; Helms, B. A.; Russell, T. P. Building Reconfigurable Devices Using Complex Liquid-Fluid Interfaces. *Adv. Mater.* **2019**, 31, DOI: 10.1002/adma.201806370.

[26] Forth, J.; Liu, X. B.; Hasnain, J.; Toor, A.; Miszta, K.; Shi, S. W.; Geissler, P. L.; Emrick, T.; Helms, B. A.; Russell, T. P. Reconfigurable Printed Liquids. *Adv. Mater.* **2018**, 30, DOI: 10.1002/adma.201707603.

[27] Lin, Y.; Skaff, H.; Emrick, T.; Dinsmore, A. D.; Russell, T. P. Nanoparticle Assembly and Transport at Liquid-Liquid Interfaces. *Science* **2003**, 299, 226-229, DOI: 10.1126/science.1078616.

[28] Khan, M. A.; Haase, M. F. Stabilizing Liquid Drops in Nonequilibrium Shapes by the Interfacial Crosslinking of Nanoparticles. *Soft Matter* **2021**, 17, 2034-2041, DOI: 10.1039/d0sm02120b.

[29] Cain, J. D.; Azizi, A.; Maleski, K.; Anasori, B.; Glazer, E. C.; Kim, P. Y.; Gogotsi, Y.; Helms, B. A.; Russell, T. P.; Zettl, A. Sculpting Liquids with Two-Dimensional Materials: The Assembly of TiCT Mxene Sheets at Liquid Liquid Interfaces. *ACS Nano* **2019**, 13, 12385-12392, DOI: 10.1021/acsnano.9b05088.

[30] Shi, S. W.; Qian, B. Q.; Wu, X. Y.; Sun, H. L.; Wang, H. Q.; Zhang, H. B.; Yu, Z. Z.; Russell, T. P. Self-Assembly of Mxene-Surfactants at Liquid-Liquid Interfaces: From Structured Liquids to 3d Aerogels. *Angew. Chem.* **2019**, 58, 18171-18176, DOI: 10.1002/anie.201908402.

[31] Beygisangchin, M.; Rashid, S. A.; Shafie, S.; Sadrolhosseini, A. R.; Lim, H. N. Preparations, Properties, and Applications of Polyaniline and Polyaniline Thin Films-a Review. *Polymers* **2021**, 13, DOI: 10.3390/polym13122003.

[32] Pan, L. J.; Yu, G. H.; Zhai, D. Y.; Lee, H. R.; Zhao, W. T.; Liu, N.; Wang, H. L.; Tee, B. C. K.; Shi, Y.; Cui, Y.; Bao, Z. Hierarchical Nanostructured Conducting Polymer Hydrogel with High Electrochemical Activity. *Proc. Natl. Acad. Sci. USA* **2012**, 109, 9287-9292, DOI: 10.1073/pnas.1202636109.

[33] Wang, Y.; Ma, W. B.; Guo, L.; Song, X. Z.; Tao, X. Y.; Guo, L. T.; Fan, H. L.; Liu, Z. S.; Zhu, Y. B.; Wei, X. Y. Phytic Acid-Doped Poly(Aniline-Co-Pyrrole) Copolymers for Supercapacitor Electrodes Applications. *J. Mater. Sci.: Mater. Electron.* **2020**, 31, 6263-6273, DOI: 10.1007/s10854-020-03181-5.

[34] Jiang, D. W.; Murugadoss, V.; Wang, Y.; Lin, J.; Ding, T.; Wang, Z. C.; Shao, Q.; Wang, C.; Liu, H.; Lu, N.; Wei, R.; Subramania, A.; Guo, Z. Electromagnetic Interference Shielding Polymers and Nanocomposites-a Review. *Polym Rev.* **2019**, 59, 280-337, DOI: 10.1080/15583724.2018.1546737.

[35] Zhao, L. J.; Zhang, H.; Tang, N.; Li, M. H.; Hu, J. Natural Phytic Acid-Assisted Polyaniline/Poly(Vinyl Alcohol) Hydrogel Showing Self-Reinforcing Features. *ACS Appl. Mater. Interfaces* **2023**, 15, 41927-41936, DOI: 10.1021/acsami.3c09032.

[36] Zhang, C. K.; Chen, Q. L.; Ai, X.; Li, X. G.; Xie, Q. S.; Cheng, Y.; Kong, H. F.; Xu, W. J.; Wang, L. S.; Wang, M. S.; Yang, H.; Peng, D. L. Conductive Polyaniline Doped with Phytic Acid as a Binder and Conductive Additive for a Commercial Silicon Anode with Enhanced Lithium Storage Properties. *J. Mater. Chem. A* **2020**, 8, 16323-16331, DOI: 10.1039/d0ta04389c.

[37] Zhou, Q. Q.; Chen, J. Y.; Zhou, T. C.; Shao, J. Z. Polymerization of Polyaniline on Cotton Fabrics with Phytic Acid as a Novel Efficient Dopant for Flame Retardancy and Conductivity Switching. *New J. Chem.* **2020**, 44, 3504-3513, DOI: 10.1039/c9nj05689k.

[38] Deo, K. A.; Jaiswal, M. K.; Abasi, S.; Lokhande, G.; Bhunia, S.; Nguyen, T. U.; Namkoong, M.; Darvesh, K.; Guiseppi-Elie, A.; Tian, L. M.; Gaharwar, A. K. Nanoengineered Ink for Designing 3d Printable Flexible Bioelectronics. *ACS Nano* **2022**, 16, 8798-8811, DOI: 10.1021/acsnano.1c09386.

[39] Zhou, K.; *Additive Manufacturing : Materials, Functionalities and Applications*; Springer International Publishing, Cham, Switzerland **2023**.

[40] Wei, X. L.; Wang, Y. Z.; Long, S. M.; Bobeczko, C.; Epstein, A. J. Synthesis and Physical Properties of Highly Sulfonated Polyaniline. *J. Am. Chem. Soc.* **1996**, 118, 2545-2555, DOI: 10.1021/ja952277i.

[41] Macdiarmid, A. G. *The Polyanilines - a Novel Class of Conducting Polymers* in Conjugated Polymers and Related Materials: The Interconnection of Chemical and Electronic Structure. 73-98. Salaneck, W. R.; Ranby, B. G., Lundstrom, I. Lulea, Sweden. **1993**.

[42] Yue, J.; Gordon, G.; Epstein, A. J. Comparison of Different Synthetic Routes for Sulfonation of Polyaniline. *Polymer* **1992**, 33, 4410-4418, DOI: 10.1016/0032-3861(92)90288-8.

[43] Ma, Z.; Shi, W.; Yan, K.; Pan, L. J.; Yu, G. H. Doping Engineering of Conductive Polymer Hydrogels and Their Application in Advanced Sensor Technologies. *Chem. Sci.* **2019**, 10, 6232-6244, DOI: 10.1039/c9sc02033k.

[44] Yan, B.; Chen, Z. H.; Cai, L.; Chen, Z. M.; Fu, J. W.; Xu, Q. Fabrication of Polyaniline Hydrogel: Synthesis, Characterization and Adsorption of Methylene Blue. *Appl. Surf. Sci.* **2015**, 356, 39-47, DOI: 10.1016/j.apsusc.2015.08.024.

[45] Ballabio, M.; Zhang, T.; Chen, C.; Zhang, P.; Liao, Z. Q.; Hambsch, M.; Mannsfeld, S. C. B.; Zschech, E.; Sirringhaus, H.; Feng, X. L.; Bonn, M.; Dong, R.; Canovas, E. Band-Like Charge Transport in Phytic Acid-Doped Polyaniline Thin Films. *Adv. Funct. Mater.* **2021**, 31, DOI: 10.1002/adfm.202105184.

[46] Cui, M. M.; Emrick, T.; Russell, T. P. Stabilizing Liquid Drops in Nonequilibrium Shapes by the Interfacial Jamming of Nanoparticles. *Science* **2013**, 342, 460-463, DOI: 10.1126/science.1242852.

[47] Liu, X. B.; Kent, N.; Ceballos, A.; Streubel, R.; Jiang, Y. F.; Chai, Y.; Kim, P. Y.; Forth, J.; Hellman, F.; Shi, S. W.; Wang, D.; Helms, B. A.; Ashby, P. D.; Fischer, P.; Russell, T. P. Reconfigurable Ferromagnetic Liquid Droplets. *Science* **2019**, 365, 264-267, DOI: 10.1126/science.aaw8719.

[48] Toor, A.; Forth, J.; de Araujo, S. B.; Merola, M. C.; Jiang, Y. F.; Liu, X. B.; Chai, Y.; Hou, H. H.; Ashby, P. D.; Fuller, G. G.; Russell, T. P. Mechanical Properties of Solidifying Assemblies of Nanoparticle Surfactants at the Oil-Water Interface. *Langmuir* **2019**, 35, 13340-13350, DOI: 10.1021/acs.langmuir.9b01575.

[49] Chai, Y.; Lukito, A.; Jiang, Y. F.; Ashby, P. D.; Russell, T. P. Fine-Tuning Nanoparticle Packing at Water-Oil Interfaces Using Ionic Strength. *Nano Lett.* **2017**, 17, 6453-6457, DOI: 10.1021/acs.nanolett.7b03462.

[50] Xu, R. Y.; Liu, T.; Sun, H. L.; Wang, B. B.; Shi, S. W.; Russell, T. P. Interfacial Assembly and Jamming of Polyelectrolyte Surfactants: A Simple Route to Print Liquids in Low-Viscosity Solution. *ACS Appl. Mater. Interfaces* **2020**, 12, 18116-18122, DOI: 10.1021/acsami.0c00577.

[51] Farrokhzad, H.; Van Gerven, T.; Van der Bruggen, B. Preparation and Characterization of a Conductive Polyaniline/Polysulfone Film and Evaluation of the Effect of Co-Solvent. *Eur. Polym. J.* **2013**, 49, 3234-3243, DOI: 10.1016/j.eurpolymj.2013.06.027.

AUTHOR INFORMATION

Corresponding Author

Thomas P. Russell, E-mail: russell@mail.pse.umass.edu.

TOC: The dense interfacial assembly of PA/S-PANI complexes at oil–water interfaces greatly increase the conductive nature of the thin films forms at the interface. PA/S-PANI inks are 3D printed into liquid threads such that liquid circuits can be fabricated into series and parallel circuits which can be repaired to pristine conditions or reconfigured into new circuits using an electric field.